Nano Research 2018, 11(9): 4823–4835
https://doi.org/10.1007/s12274-018-2070-4
Research Article

ISSN 1998-0124
CN 11-5974/O4

Conformal and continuous deposition of bifunctional cobalt phosphide layers on p-silicon nanowire arrays for improved solar hydrogen evolution

Sitaramanjaneva Mouli Thalluri[1], Jerome Borme[1], Kang Yu[1,2], Junyuan Xu[1], Isilda Amorim[1], Joao Gaspar[1], Liang Qiao[3], Paulo Ferreira[1,2,4], Pedro Alpuim[1,5], and Lifeng Liu[1] (✉)

[1] *International Iberian Nanotechnology Laboratory (INL), Av. Mestre. Jose Veiga, Braga 4715-330, Portugal*
[2] *Materials Science and Engineering Program, University of Texas at Austin, Austin TX78712, USA*
[3] *Department of Chemistry, State Key Laboratory of Molecular Engineering of Polymers and Institute of Biomedical Sciences, Fudan University, Shanghai 200433, China*
[4] *Mechanical Engineering Department and IDMEC, Instituto Superior Técnico,University of Lisbon, Av. Rovisco Pais, Lisboa 1049-001, Portugal*
[5] *Center of Physics, University of Minho, Braga 4710-057, Portugal*

Received: 16 January 2018
Revised: 22 March 2018
Accepted: 7 April 2018

KEYWORDS

solar-driven hydrogen evolution,
silicon nanowire,
cobalt phosphide,
photoelectrochemical water splitting,
drop-casting

ABSTRACT

Vertically aligned p-silicon nanowire (SiNW) arrays have been extensively investigated in recent years as promising photocathodes for solar-driven hydrogen evolution. However, the fabrication of SiNW photocathodes with both high photoelectrocatalytic activity and long-term operational stability using a simple and affordable approach is a challenging task. Herein, we report conformal and continuous deposition of a di-cobalt phosphide (Co_2P) layer on lithography-patterned highly ordered SiNW arrays via a cost-effective drop-casting method followed by a low-temperature phosphorization treatment. The as-deposited Co_2P layer consists of crystalline nanoparticles and has an intimate contact with SiNWs, forming a well-defined SiNW@Co_2P core/shell nanostructure. The conformal and continuous Co_2P layer functions as a highly efficient catalyst capable of substantially improving the photoelectrocatalytic activity for the hydrogen evolution reaction (HER) and effectively passivates the SiNWs to protect them from photo-oxidation, thus prolonging the lifetime of the electrode. As a consequence, the SiNW@Co_2P photocathode with an optimized Co_2P layer thickness exhibits a high photocurrent density of $-21.9\ \text{mA}\cdot\text{cm}^{-2}$ at 0 V versus reversible hydrogen electrode and excellent operational stability up to 20 h for solar-driven hydrogen evolution, outperforming many nanostructured silicon photocathodes reported in the literature. The combination of passivation and catalytic functions in a single continuous layer represents a promising strategy for designing high-performance semiconductor photoelectrodes for use in solar-driven water splitting, which may simplify fabrication procedures and potentially reduce production costs.

Address correspondence to lifeng.liu@inl.int

1 Introduction

The ever-growing global population has caused a huge demand for energy. To prevent depletion of non-renewable fossil fuels and to alleviate the serious environmental pollution associated with consumption of fossil fuels, a consensus has been reached that renewable energy sources should be employed on a large scale and should steadily replace fossil fuels until they dominate the global energy supply [1]. Converting solar energy into storable and clean chemical fuels such as hydrogen (H_2) through photoelectrochemical (PEC) water splitting represents a promising and sustainable approach to solar energy utilization and storage and has regained considerable research interest in recent years [2–5]. To make PEC-derived H_2 economically competitive and affordable, low-cost and earth-abundant yet highly efficient semiconductors and electrocatalysts must be used. In this regard, Si stands out among the other semiconductor materials, because it is the second most abundant element on the earth's crust and inexpensive. It has a band gap of 1.12 eV, which enables light absorption over a wide range of the solar spectrum. Furthermore, the conduction band edge of Si is positioned negatively relative to the proton reduction potential at the reversible hydrogen electrode (RHE) scale, which is the right position for charge transfer when driving the hydrogen evolution reaction (HER) [6, 7]. Moreover, the processing techniques of Si are well established and can be readily used in photoelectrode development [8]. In terms of electrocatalysts, Pt is the most efficient for HER. However, the prohibitive cost and scarcity of Pt are the major limiting factors for large-scale applications of this efficient catalyst. Therefore, many recent research works have focused on non-precious transition metal based HER catalysts including chalcogenides [9–18], phosphides [19–27], carbides [28–30], borides [31, 32], and nitrides [33], and their HER performances have been reported to be favorably comparable to that of Pt.

In the last few years, unremitting efforts have been made to improve the PEC performance of Si based photocathodes by either nanostructuring Si or coupling efficient HER catalysts with Si or a combination of both strategies [9, 34–39]. However, in many cases, the catalysts only sparsely cover the surface of Si micro-/nanostructured photoelectrodes [21, 22, 40–43], and the Si surface exposed to aqueous electrolyte gets oxidized over time, eventually leading to device failure. This has posed a great challenge for practical applications of Si-based photoelectrodes in solar-driven H_2 evolution. To overcome this problem, a chemically inert passivation layer (e.g., TiO_2) was introduced to prevent Si from photo-oxidation, followed by coupling of HER catalysts on the deposited passivation layer to improve the H_2 production rate [34, 40, 44–46]. This Si/passivation layer/catalyst configuration has been demonstrated to be able to substantially improve the lifetime of Si-based photoelectrodes; nevertheless, the photocurrent generated will be compromised in many cases, because of the loss of electrons during tunneling across the passivation layer [47].

Herein, we report conformal and continuous deposition of a di-cobalt phosphide (Co_2P) layer on highly ordered Si nanowire (SiNW) arrays using a simple and cost-effective drop-casting method, followed by a post-phosphorization treatment. This single Co_2P layer performs dual functions: On the one hand, it can efficiently catalyze the HER owing to its high electrocatalytic activity, which has been extensively demonstrated recently [21, 23, 26, 48, 49]; on the other hand, it functions as an effective passivation layer protecting SiNWs from photo-oxidation during long-term operation. The as-fabricated SiNW@Co_2P core/shell photocathodes exhibited a high photocurrent density of $-21.9\ \text{mA}\cdot\text{cm}^{-2}$ at 0 V vs. RHE in 0.5 M H_2SO_4 and were stable under PEC operation conditions for 20 h without significant degradation.

2 Results and discussion

The SiNWs were fabricated by standard e-beam lithography and subsequent deep reactive ion etching (DRIE) processes, as described in the Experimental section. The as-fabricated SiNWs have a wavy side wall, which results from the alternate passivation and etching steps during the DRIE process. Similar structural features were observed previously as well in Si microwires (SiMWs) fabricated by the top-down RIE process [9, 50]. It is to be noted that nanostructuring does not change the band gap of Si, and SiNW arrays show a band gap of ca. 1.1 eV according to the Tauc plot (Fig. S1 in the

Electronic Supplementary Material (ESM)), which is the same as that of planar Si. To incorporate the cobalt phosphide layer, a mixed solution of cobalt acetate and ethanol with different concentrations of Co^{2+}, ranging from 2.25 to 62 mM, was drop-cast on the surface of the SiNW arrays and dried at ambient conditions. A phosphorization treatment was then performed in a tube furnace using red phosphorous as the source of phosphorous (see Experimental section). All the steps involved in the process of fabrication are schematically illustrated in Fig. 1.

Figures 2(b)–2(d) show typical scanning electron microscopy (SEM) images of the SiNW@Co_2P photoelectrodes prepared using Co^{2+} concentrations of 9, 18, and 36 mM (denoted as SiNW@Co_2P-X, X = 9, 18, and 36). No discernable differences are found between the appearances of SiNW@Co_2P-X ($X \leq 9$ mM) and the as-fabricated SiNW array (Fig. 2(a) and Fig. S2 in the ESM). However, the diameter of the NWs increases as the Co^{2+} precursor concentration is increased to 18 and 36 mM, and certain irregular particles are found to be deposited on the side walls of the NWs (Figs. 2(c) and 2(d)). Moreover, it is observed that the parent Si substrate is covered with a thick layer of Co_2P. In appearance, SiNW@Co_2P-18 and SiNW@Co_2P-36 are darker than SiNW@Co_2P-X ($X \leq 9$ mM).

X-ray diffraction (XRD) studies were carried out to examine the crystallinity of the deposited cobalt phosphide layer. Only very weak diffraction peaks from Co_2P (ICDD No. 00-032-0306) are observed for the SiNW@Co_2P photocathodes prepared with a Co^{2+} precursor concentration of 4.5 mM and above (Fig. S3 in the ESM). This indicates that either the deposited layer is poorly crystallized or the crystallite size of Co_2P is too small for characterization by XRD. To gain further insight into the microstructure of the deposited layer, transmission electron microscopy (TEM) studies were carried out. Figure 3(a) shows a montage TEM image of a single SiNW@Co_2P-9, wherein a continuous layer conformally coats the entire surface of the NW, forming a core/shell nanostructure. A closer look at the NW surface shows that the coating layer consists of many nanoparticles (NPs; Fig. 3(b)). These NPs have typical diameters ranging from 3 to 6 nm and are highly crystalline, as confirmed by the high-resolution TEM (HRTEM) image shown in Fig. 3(c). Selected-area electron diffraction (SAED) analysis of the NPs in Fig. 3(d) shows a well-defined ring pattern, which can be exclusively indexed as the orthorhombic phase of Co_2P (ICDD No. 00-032-0306). It is also evident that the thickness of the Co_2P layer varies from the top to the bottom of the NW. This non-uniformity is believed to result from the uneven distribution of the precursor solution during the drop-casting process, driven by the gravimetric effect. The non-uniform layer thickness is resolved more clearly in the signal map of Co_2P along the NW, as displayed in Fig. 3(e), which shows that Co_2P is more predominant around the root of the NW than at the top (see also energy-dispersive X-ray spectroscopy (EDS) results in Fig. S4 in the ESM).

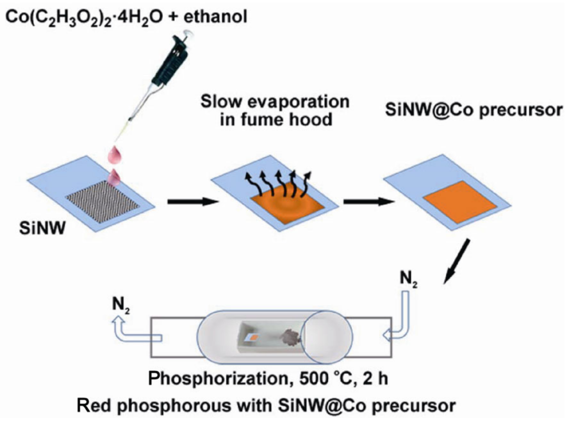

Figure 1 Schematic illustration of the fabrication of the SiNW@Co_2P photocathodes.

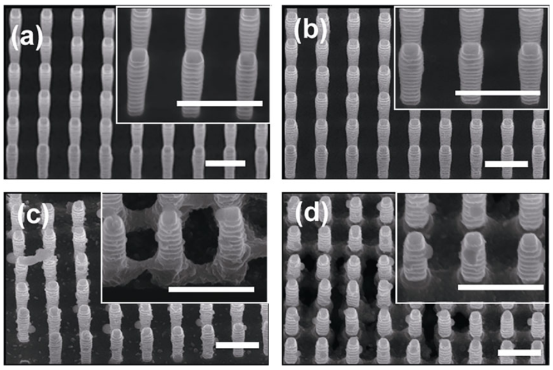

Figure 2 SEM images showing the morphologies of the (a) as-fabricated SiNW arrays and the SiNW@Co_2P photocathodes prepared with Co precursor concentrations of (b) 9, (c) 18, and (d) 36 mM. Scale bars: 500 nm.

To further investigate the distribution of Co and P elements on the surface of the SiNWs, elemental mapping was performed in high-angle annular dark-field

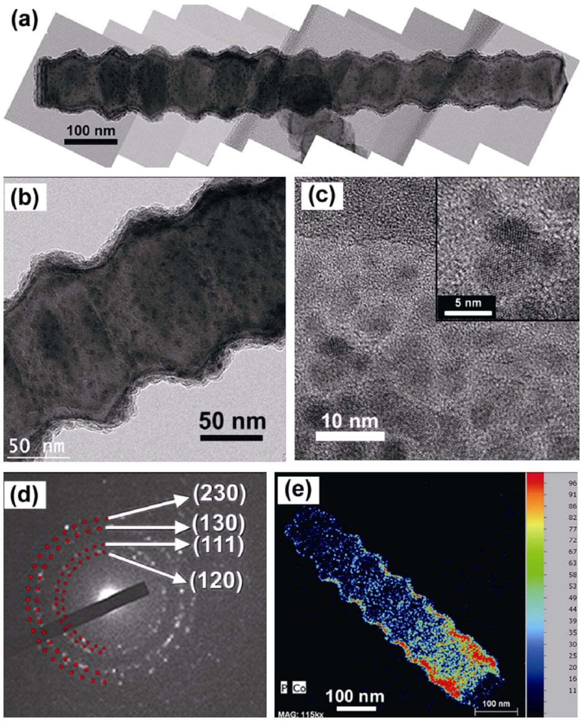

Figure 3 (a) Montage TEM image showing conformal and continuous deposition of the Co_2P layer on SiNW. (b) and (c) High-magnification TEM images of SiNW@Co_2P; the inset in (c) shows the HRTEM image. (d) SAED pattern of the Co_2P NPs. (e) EDS signal map showing the distribution of Co_2P along the SiNW. The intensity of Co_2P is more predominant around the root than at the top.

scanning TEM (HAADF-STEM) mode. Figure 4(a) shows the representative HAADF-STEM image of SiNW@Co_2P wherein the particulate feature of Co_2P is observed more clearly. As revealed by the elemental maps in Figs. 4(b)–4(e), both Co and P are continuously and conformally deposited on the surface of the SiNW, resulting in a core/shell structure, which agrees well with the bright-field TEM observation (Fig. 3(a)). This indicates that solution-based drop-casting is an effective method for coating nanostructured photoelectrodes with a thin conformal passivation/catalyst layer.

To examine the chemical states of the deposited Co_2P layer, X-ray photoelectron spectroscopy (XPS) was performed. The XPS survey spectrum shows the co-existence of Co, P, and Si, consistent with the EDS results (Fig. S4 in the ESM). The presence of other elements (i.e., C, N, and O) is attributed to adventitious absorption during exposure of the electrode to air at atmospheric conditions (Fig. 5(a)). Figure 5(b) shows the high-resolution XPS spectrum of the Co 2p core level, in which two major peaks of Co $2p_{3/2}$ are observed at binding energy (BE) values of 779.0 and 781.8 eV. The BE values of the peaks are positively shifted relative to that of metallic Co (778.2 eV), indicating an electron density transfer from Co atoms to P atoms in Co_2P. The peaks located at 785.4 and 788.6 eV are the satellite peaks of Co $2p_{3/2}$. Figure 5(c) shows the high-resolution XPS spectrum of P 2p core level, in which the peaks at 129.3 and 130.5 eV correspond to P $2p_{3/2}$ and P $2p_{1/2}$, respectively, in agreement with the previously reported values for Co_2P [51]. The BE value of P $2p_{3/2}$ (129.3 eV) is lower than that of elemental P (130.0 eV), confirming the partial electron density transfer from Co atoms to P atoms in the deposited Co_2P. As a result, the P centers may promote the formation of cobalt hydride, which would then facilitate the hydrogen evolution process by electrochemical

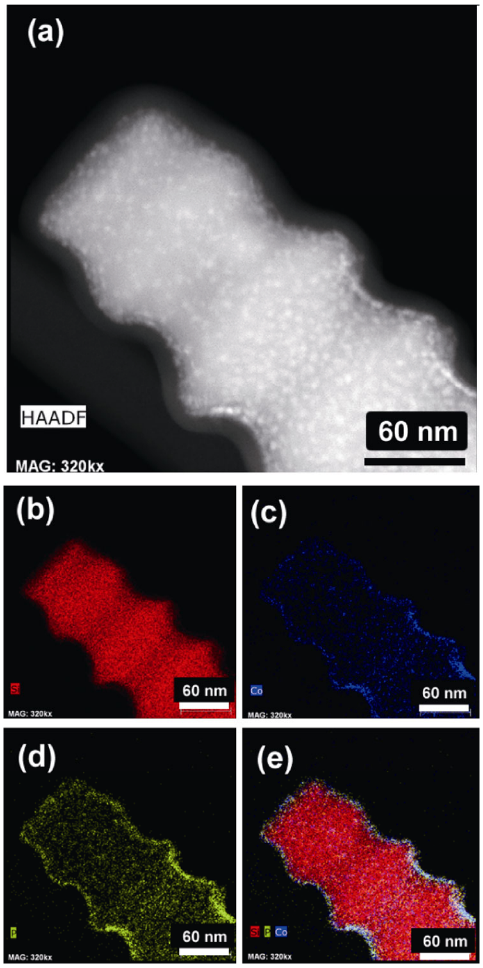

Figure 4 (a) HAADF-STEM image of an individual SiNW@Co_2P and the elemental maps of (b) Si, (c) Co, (d) P, and (e) their overlay.

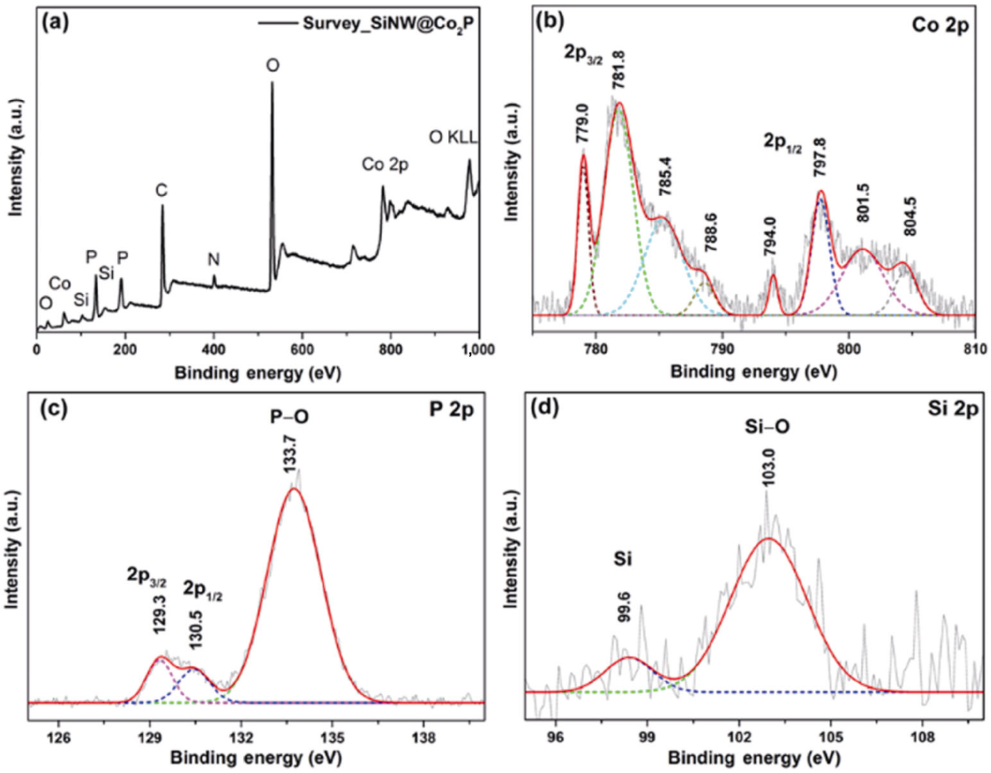

Figure 5 (a) Representative XPS survey spectrum and high resolution XPS spectra of (b) Co 2p, (c) P 2p, and (d) Si. The grey curves represent the experimentally measured spectra, the solid red lines are the fitting curves of the whole spectra, and the colored dash lines represent the fitting curves of each BE peak.

desorption. In addition to the peaks arising from phosphide, the peak observed at 133.7 eV can be assigned to the P–O bond, which may result from the surface oxidation of Co_2P upon exposure to air; this is also commonly observed in other phosphides reported previously [52, 53]. The Si 2p XPS spectrum presented in Fig. 5(d) shows two peaks located at 99.6 and 103.0 eV, which are assigned to elemental Si and Si–O bond, respectively. The Si–O bond may originate from either native oxide of Si, or reaction between Si and the drop-cast precursor solution (i.e., $Co(OAc)_2$) during the phosphorization process.

The PEC performance of the SiNW@Co_2P photocathodes was comprehensively assessed in the three-electrode configuration in 0.5 M H_2SO_4 (pH = 0.3) under 100 mW·cm^{-2} illumination using linear scan voltammetry (LSV), Mott–Schottky (M–S) analysis, electrochemical impedance spectroscopy (EIS), and chronoamperometry (CA). For comparison, Pt NP decorated SiNW arrays (i.e., SiNW@Pt) were also fabricated and tested under the same conditions (see Experimental section for details). Figure 6(a) shows the LSV curves of the bare SiNW, SiNW@Pt, and SiNW@Co_2P-X (X = 2.25, 4.5, and 9 mM) photocathodes on the RHE scale. The LSV curves of the other SiNW@Co_2P-X samples are presented in Fig. S5 in the ESM. The bare SiNW photocathode generates a negligible photocurrent at 0 V vs. RHE (ca. –0.1 mA·cm^{-2}) and shows an onset potential (U_{onset}, defined as the potential at which the cathodic photocurrent density is –0.5 mA·cm^{-2}) of –0.14 V vs. RHE. Upon coupling with the Co_2P catalyst, the onset potentials of the SiNW@Co_2P-X photocathodes are significantly shifted toward the positive direction, reaching +0.24, +0.25, and +0.20 V vs. RHE for SiNW@Co_2P-2.25, SiNW@Co_2P-4.5, and SiNW@Co_2P-9, respectively. The positive shift of the onset potential, which is ascribed to suppression of recombination of photogenerated charge carriers, has been reported previously for Si-based photocathodes coupled with HER catalysts [34]. Besides, the photocurrent density at 0 V vs. RHE (J_0) of the SiNW@Co_2P-X photocathodes is substantially enhanced to –7.4, –21.9, and –12.2 mA·cm^{-2} for SiNW@Co_2P-2.25, SiNW@Co_2P-4.5, and SiNW@Co_2P-9, respectively. Among all the samples investigated,

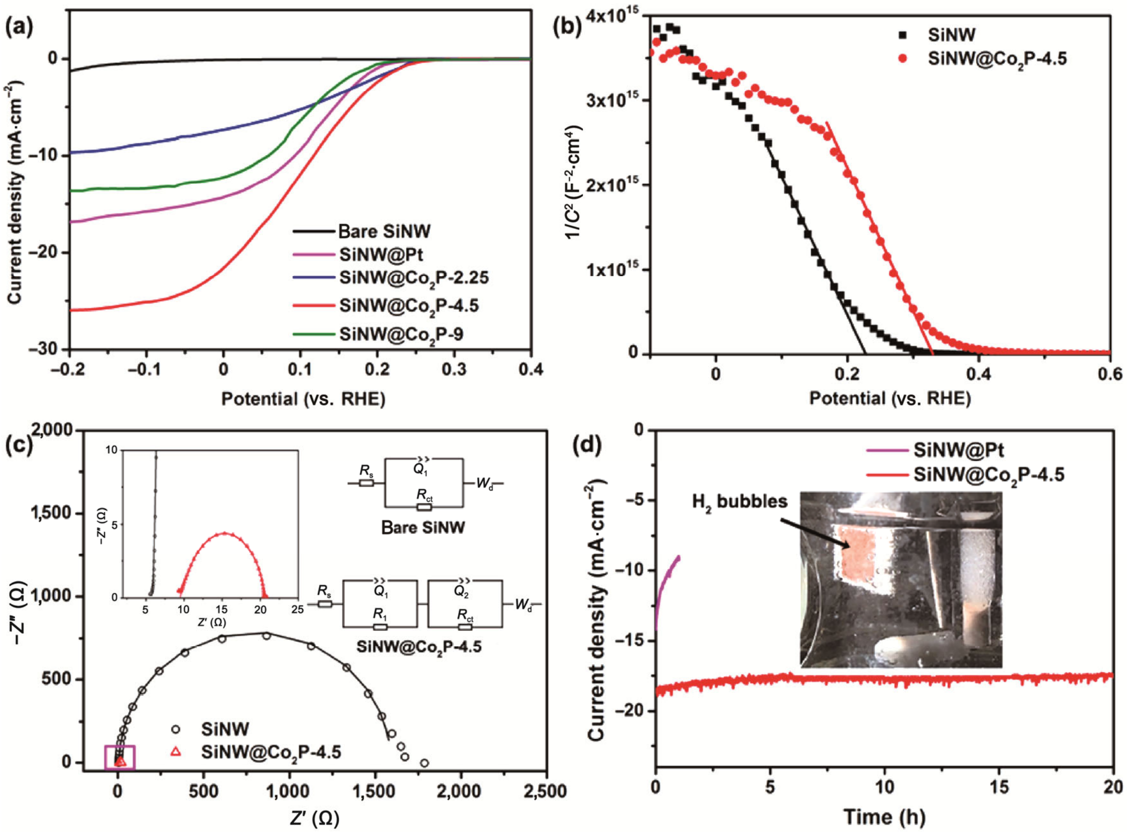

Figure 6 (a) Linear scan voltammograms of the bare SiNW, SiNW@Pt, and SiNW@Co_2P photocathodes recorded under 100 mW·cm^{-2} illumination. (b) Mott–Schottky plots of the bare SiNW and the SiNW@Co_2P-4.5 photocathodes measured in the dark at 10 kHz. (c) Nyquist plots of the bare SiNW and the SiNW@Co_2P-4.5 photocathodes recorded at +0.15 V vs. RHE under 100 mW·cm^{-2} illumination. The insets show the enlarged view in the high frequency region (left) and the equivalent circuit models (right). (d) Long-term stability tests conducted at 0 V vs. RHE for the SiNW@Pt and the SiNW@Co_2P-4.5 photocathodes. All the measurements were carried out in 0.5 M H_2SO_4 solution at room temperature.

SiNW@Co_2P-4.5 exhibits the best photoelectrocatalytic performance; it is not only better than the SiNW@Pt control sample, which exhibits U_{onset} of +0.21 V vs. RHE and J_0 of –14.4 mA·cm^{-2}, but also outperforms many Si-based photocathodes reported previously in the literature (Table S1 in the ESM), such as MoO_xS_y decorated SiMW arrays (U_{onset} = +0.24 V and J_0 = –9.83 mA·cm^{-2}) [9], reduced graphene oxide-decorated SiNWs (U_{onset} = +0.206 V and J_0 = –3 mA·cm^{-2}) [54], MoS_2-wrapped SiNWs (U_{onset} = +0.3 V and J_0 = –15 mA·cm^{-2}) [13], W_2C modified SiNWs (U_{onset} = +0.2 V and J_0 = –16 mA·cm^{-2}) [30], and SiMW@cobalt dichalcogenide (U_{onset} = +0.29 V and J_0 = –3.22 mA·cm^{-2}) [15]. The SiNW@Co_2P photocathodes prepared with precursor concentrations higher than 9 mM were also tested (Fig. S5 in the ESM), and the values of J_0 and limiting photocurrent density of these photocathodes were found to decrease with increase in the precursor concentration. This might result from the increase in series resistance due to carrier depletion resulting from the reduced light absorption by the SiNW electrodes as a consequence of the increased thickness of the Co_2P layer. Besides, the loading density of Co_2P on the SiNW arrays was roughly estimated (see Experimental section for details), and the dependence of J_0 and U_{onset} on the Co_2P loading is plotted in Fig. S6 in the ESM. The best-performing SiNW@Co_2P-4.5 photocathode has an optimal Co_2P loading of ca. 13.4 μg·cm^{-2}, without considering the possible loss of Co during both the drop-casting and the phosphorization processes.

The capacitance-voltage measurements were performed in the dark in 0.5 M H_2SO_4 at a frequency of 10 kHz to further investigate the flat band potential (U_{fb}) of the photocathodes. Figure 6(b) shows the M–S plots of the bare SiNW arrays and the best-performing

SiNW@Co_2P-4.5 electrodes. Both SiNW and SiNW@Co_2P-4.5 show a negative M–S slope, characteristic of p-type semiconductors. The value of U_{fb} can be calculated using the following M–S equation [54]

$$\frac{1}{C^2} = 2\frac{U_a - U_{fb} - \frac{kT}{q}}{qN_d\varepsilon_s\varepsilon_0 A^2} \tag{1}$$

where C is the space charge capacity, U_a is the applied potential, k represents the Boltzmann constant, T is the absolute temperature, q is the electron charge, N_d is the donor density, ε_s is the dielectric constant of materials, ε_0 is the electric permittivity of vacuum, and A is the surface area. The band bending (U_b) of semiconductor photoelectrodes can be determined by the applied potential and U_{fb} through Eq. (2) [54, 55]

$$U_b = U_a - U_{fb} \tag{2}$$

Since U_a is negative under the cathodic reaction for proton reduction, a large U_{fb} will lead to a large absolute value of U_b; i.e., a photocathode having a more positive U_{fb} will exhibit a larger band bending. As a result, the separation of photogenerated electrons and holes will be faster at the electrode/electrolyte interface, and consequently, the surface charge trapping and recombination can be largely suppressed. According to Fig. 6(b), the U_{fb} of SiNW and SiNW@Co_2P-4.5 is +0.23 and +0.33 V vs. RHE, respectively, suggesting that a larger band bending was achieved for the SiNW@Co_2P-4.5 photocathode. This explains the reason for the remarkably large values of U_{onset} and J_0 of the SiNW@Co_2P photocathodes.

The charge transfer kinetics at the interface between the electrolyte and bare SiNW or SiNW@Co_2P-4.5 was further studied at +0.15 V vs. RHE using EIS under 100 mW·cm^{-2} illumination. Figure 6(c) shows the EIS Nyquist plots of the SiNW and the SiNW@Co_2P-4.5 photocathodes. The Nyquist plots are fitted with the equivalent circuit models, as shown in the insets of Fig. 6(c), where R_s represents the equivalent series resistance, W_d is the Warburg resistance arising from diffusion in the NW arrays, Q_1 and Q_2 are the constant phase elements, R_1 is the charge transport resistance at the interface between SiNW and Co_2P layer, and R_{ct} is the resistance of charge transfer at the electrode/electrolyte interface. As revealed in the enlarged view of the Nyquist plots in the insets of Fig. 6(c), R_s of the SiNW@Co_2P-4.5 photocathode increases after coupling with the Co_2P layer as a consequence of the introduction of the Co_2P layer. Nevertheless, R_{ct} of the SiNW@Co_2P-4.5 electrode is significantly reduced to 10.3 Ω, ca. 150 times smaller than that of the bare SiNW photocathode (R_{ct} = 1,583 Ω, Table S2 in the ESM). This indicates that the deposited Co_2P catalyst layer substantially expedites the charge transfer kinetics of SiNWs during solar-driven hydrogen evolution, which is consistent with the above M–S analysis.

Long-term stability under PEC operation conditions is of essential importance for practical deployment of PEC devices for solar-driven hydrogen production. Without appropriate passivation, Si-based photocathodes will be photo-oxidized in a short period of time even in a strong acidic (i.e., reductive) solution, leading to failure of devices [34, 47]. Presently, the most commonly used passivation strategy is to coat Si-based photoelectrodes with a continuous layer of wide-band-gap semiconductor (e.g., TiO_2, SiO_2, etc.) that not only allows for the penetration of incident light but also has excellent chemical stability and enables tunneling for the transport of photogenerated charge carriers [40, 56, 57]. Recently, some researchers demonstrated that a continuous layer of HER catalysts with sufficient electrochemical stability can effectively protect Si from oxidation [9, 23] besides helping to promote the HER, thus offering dual functions. Co_2P has been widely reported to have good electrochemical stability when used as an HER catalyst [49], and is therefore a good choice of material. Figure 6(d) shows the CA curves of the SiNW@Co_2P-4.5 and the SiNW@Pt photocathodes recorded at 0 V vs. RHE under 100 mW·cm^{-2} illumination in 0.5 H_2SO_4. It is evident that, in the CA mode, the photocurrent density at 0 V vs. RHE slightly decreases compared to the J_0 value measured by LSV. This is likely because the H_2 bubbles constantly generated during the potentiometric electrolysis (inset of Fig. 6(d), see also Movie ESM1), unlike those produced transiently during the LSV measurements, may block some of the active surface regions of the photocathode and/or scatter the incident light, leading to attenuated light absorption of the SiNW arrays. As shown in Fig. 6(d), the photocurrent density of the SiNW@Co_2P photocathode only shows a slight decrease in the initial

3 h and then gets stabilized at 17.9 mA·cm^{-2} for 20 h without significant degradation, exhibiting superior operational stability. In stark contrast, the photocurrent density of the SiNW@Pt photocathode diminishes quickly from the initial –14.2 to –9.2 mA·cm^{-2} within 1 h. Despite its high activity for the HER, Pt has been reported to exhibit poor electrochemical stability in harsh acidic or alkaline solutions owing to the high mobility of Pt atoms under electrochemical conditions [58].

The morphology, microstructure, and surface chemical states of the SiNW@Co$_2$P photocathodes were investigated by SEM, TEM, and XPS after the extended stability test. As shown in Fig. 7(a), all the SiNWs remain on the surface of the photocathode and maintain their vertical alignment with respect to the Si substrate, exhibiting a morphology similar to that observed in the as-fabricated SiNW@Co$_2$P photocathodes (Fig. 2 and Fig. S2 in the ESM). Microscopically, Co and P still exist on the surface of the SiNWs in a conformal and continuous manner, as revealed by HAADF-STEM elemental mapping analysis (Fig. 7(b)). However, the O content of the tested photocathode is significantly increased compared to

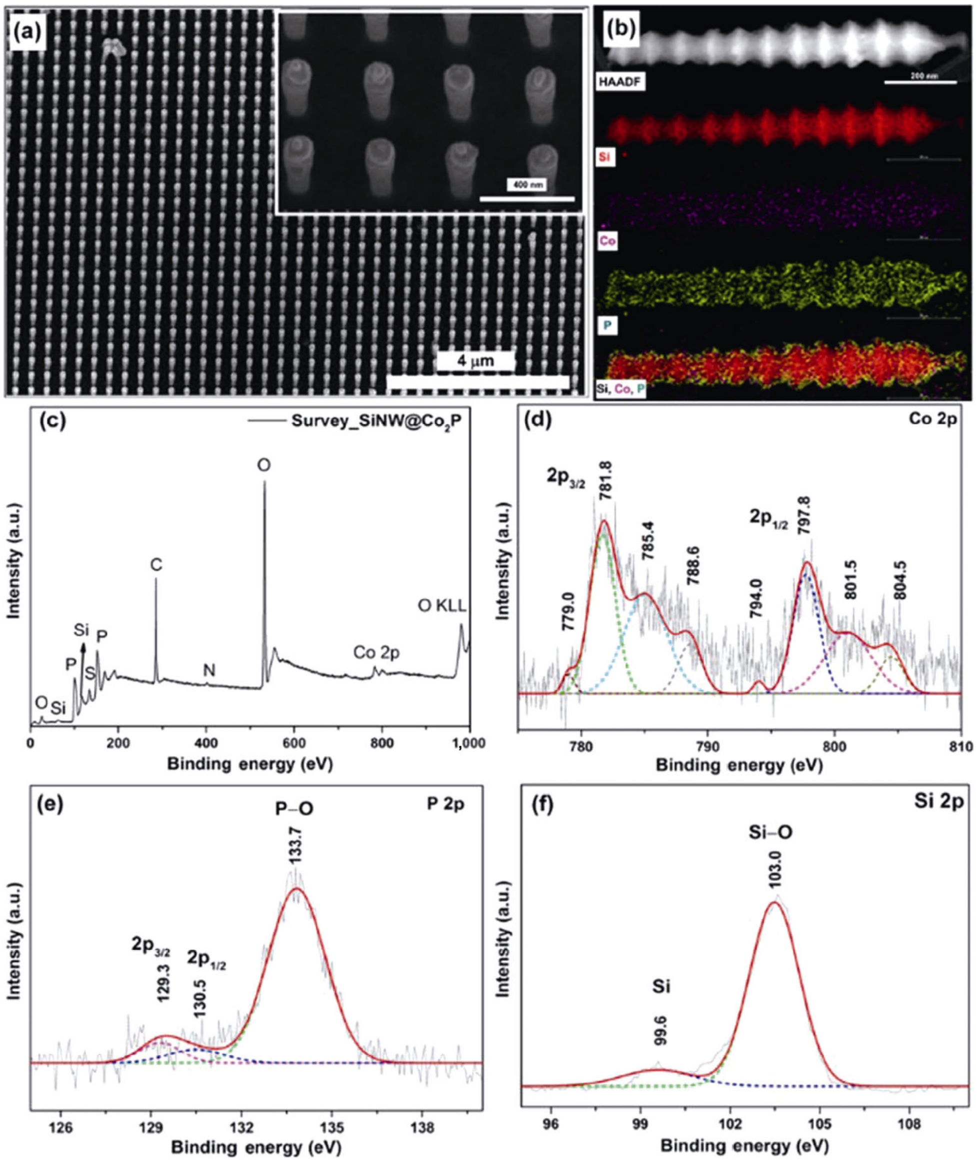

Figure 7 Morphology, microstructure, and surface chemistry of the SiNW@Co$_2$P photocathodes after the extended stability test. (a) SEM image. The inset shows the enlarged view. (b) STEM-HAADF image and EDX elemental maps of Si, Co, P, and their overlay, taken from a single SiNW@Co$_2$P after the stability test for 20 h (0 V vs. RHE in 0.5 M H_2SO_4 at 1-Sun). (c) XPS survey spectrum and high-resolution XPS spectra of (d) Co 2p, (e) P 2p, and (f) Si 2p.

that of the as-prepared SiNW@Co_2P (Fig. S4 in the ESM), as shown in the EDS spectra (Fig. S7 in the ESM). This may be attributed to the remnant SO_4^- groups introduced during the stability test or slight surface oxidation. After the stability test, the XPS spectra of the SiNW@Co_2P photocathode show characteristic peaks similar to those observed in the electrode prior to the test (Fig. 5), except for the presence of S which is believed to have originated from the adsorption of SO_4^-. In addition, the intensities of the peaks associated with Co–P bonding (i.e., 779.0 eV in the Co 2p spectrum and 129.3 eV in the P 2p spectrum) are attenuated, indicating that the outermost Co_2P is converted to cobalt phosphate.

3 Conclusions

We have fabricated SiNW@Co_2P core/shell nanostructured photocathodes based on simple and cost-effective drop-casting of a precursor solution on lithography-patterned SiNW arrays, followed by a post-phosphorization treatment at an elevated temperature. The deposited Co_2P is conformal and continuous and can serve both as a passivation layer to protect Si from photo-oxidation and as a catalyst layer to promote hydrogen evolution reaction, showing favorable bi-functionality. Upon optimizing the drop-casting conditions, the best-performing SiNW@Co_2P photocathode exhibited a hydrogen evolution onset potential of +0.25 V vs. RHE, a photocurrent density as high as $-21.9\ mA\cdot cm^{-2}$ at 0 V vs. RHE, and an excellent catalytic stability of 20 h under PEC hydrogen evolution conditions, outperforming many nanostructured Si photocathodes reported in the literature. Combining passivation and catalytic functions in a single continuous layer is a promising strategy for designing high-performance photoelectrodes as it can simplify fabrication procedures and potentially reduce production costs. It is believed that the PEC hydrogen evolution performance can be further improved by using SiNW electrodes with buried p-n junctions and by coupling with a continuous layer of catalytically active and electrochemically stable HER catalysts.

4 Experimental section

4.1 Fabrication of highly-ordered SiNW arrays

The SiNW arrays were fabricated using e-beam lithography followed by DRIE of Si. Initially, a 200 nm thick AlCuSi film was sputter-coated (Singulus Timaris FTM) on the unpolished side of a p-type Si (100) wafer (Boron doped, 1–30 Ω·cm, LG Silitron). A layer of 300 nm-thick SiO_2 was then deposited on the polished surface of the Si wafer by plasma-enhanced chemical vapor deposition (STPS MPX CVD). Subsequently, a layer of negative photoresist (ARN 7520, 200 nm thickness) was spin-coated over the deposited SiO_2. Well-ordered arrays (7 mm × 7 mm) with a square pillar size of 150 nm and a pitch of 225 nm (center to center spacing) were patterned by e-beam lithography (Vistec EBPG 5200) over the whole wafer. The pattern was developed and transferred into the underlying SiO_2 layer by RIE (SPTS APS ICP) to form a SiO_2 mesh mask for the subsequent DRIE process (SPTS Pegasus IDP) to obtain SiNW arrays of 1 μm length. Subsequently, a cleaning process was carried out using oxygen plasma (PVA TEPLA Plasma Asher) for 15 min. Then, the SiO_2 layer on top of the SiNWs was removed using an HF vapor etcher (SPTS uEtch System). The Si wafer was diced into 12 mm × 20 mm pieces using a dicing saw (DISCO DAD 3350), with the patterned area (7 mm × 7 mm) at the center of each piece. The Ohmic contact between AlCuSi and the Si wafer was made by thermally annealing the as-diced pieces at 400 °C in high-purity nitrogen (N_2, 99.999%) for 1 min at a ramping rate of $2\ ^\circ C\cdot min^{-1}$.

4.2 Fabrication of SiNW@Co_2P and SiNW@Pt

The drop-casting technique was used to deposit Co precursors onto SiNWs. The drop-casting solution contained varying concentrations of $(CH_3COO)_2Co\cdot 4H_2O$ (Sigma-Aldrich) in ethanol (Sigma-Aldrich). The solution was stirred for 15–20 min until a clear pink solution was obtained. The solution was then drop-cast over the patterned SiNW electrode using a micropipette (20 μL), and the Si photoelectrode was subsequently placed in a fume hood for slow evaporation of ethanol. Phosphorization was carried out in a tube furnace using red phosphorus (Sigma-Aldrich) as the phosphorus source. The Si substrate was placed in a ceramic boat with 0.5 g of red P placed at the upstream side. The furnace was ramped to 500 °C at a rate of $10\ ^\circ C\cdot min^{-1}$, maintained at this temperature for 2 h, and then cooled down naturally to room temperature.

A constant N_2 flow of 800 sccm was maintained through the work tube during the whole process. Assuming that all the Co species in the precursor solution were converted to Co_2P, the loading density of Co_2P ($\mu g \cdot cm^{-2}$) on the SiNW arrays can be estimated as follows

$$M(\mathrm{Co_2P}) = \frac{M_{\mathrm{W}}(\mathrm{Co_2P}) \times \frac{C \times V}{2}}{S} = \frac{148.8\ (\mathrm{g \cdot mol^{-1}}) \times \frac{C\ (\mathrm{mmol \cdot L^{-1}}) \times 20\ \mu\mathrm{L}}{2}}{0.5\ \mathrm{cm}^2} \quad (3)$$

where M is the loading density of Co_2P ($\mu g \cdot cm^{-2}$), $M_W = 148.8\ g \cdot mol^{-1}$ represents the molar weight of Co_2P, C stands for the mole concentration of the cobalt precursor solution, $V = 20\ \mu L$ is the nominal volume of the precursor solution loaded on the photocathode, and $S = 0.5\ cm^2$ is the geometric surface area of the SiNW arrays. It is to be noted that this estimation is very rough, because it does not consider the unknown loss of Co during both the drop-casting and the phosphorization processes.

Pt decorated SiNW photocathodes (SiNW@Pt) were fabricated by electroless deposition of Pt on SiNWs under calibrated 1-sun conditions in a mixture of 0.001 M K_2PtCl_6 in dilute HF (H_2O:HF = 1:50; 48% HF, Sigma-Aldrich) solution for 1 min.

4.3 Characterization

The morphology and the microstructure of the samples were examined by SEM (FEI Quanta FEG 650) and aberration-corrected TEM (FEI Titan ChemiSTEM operating at 200 keV). For the TEM observations, the nanowires were scratched off the Si substrate and directly dispersed on a lacey carbon copper grid using water as a medium. The grid was then dried at 80 °C in a vacuum oven. The surface chemistry of the samples was probed by XPS using an ESCALAB 250 Xi system (Thermo Scientific) equipped with a monochromated Al Kα X-ray source, hemispherical electron energy analyzer, magnetic lens, and video camera for viewing the analysis position. The measurements were performed at room temperature in an ultra-high vacuum chamber with a base pressure $< 5 \times 10^{-10}$ mbar. The aliphatic C 1s peak was observed at 284.6 eV. Avantage software package (Thermo Fisher Scientific) was used to fit the elemental spectra.

4.4 Photoelectrochemical tests

The PEC performance of the SiNW@Co_2P electrodes was evaluated in a three-electrode configuration with a graphite rod as the counter electrode and a saturated calomel electrode (SCE) as the reference. The electrolyte consisted of 0.5 M H_2SO_4 (Sigma-Aldrich) with a pH value of 0.3. The PEC tests were carried out in a jacketed quartz cell having a round flat window of quartz. A calibrated 1-sun solar simulator with a built-in AM 1.5 filter (Oriel® LCS-100™) was used as the light source. The LSV, EIS, M–S analysis, and chronoamperometry studies were performed using a Zennium electrochemical workstation (Zahner). The EIS measurements were conducted in the frequency range of 10 mHz–200 kHz at a fixed potential of +0.15 V vs. RHE under a nominal illumination of 100 $mW \cdot cm^{-2}$ with an AC voltage amplitude of 10 mV. The sample temperature was maintained at 23 °C by circulating water through the water jacket of the PEC cell during the test using a refrigerated chiller (HAAKE Phoenix II, Thermo Scientific). Unless otherwise stated, all the potentials are reported versus RHE by converting the potentials measured versus SCE through Eq. (4)

$$U_{\mathrm{RHE}} = U_{\mathrm{SCE}} + 0.241 + 0.059 \times \mathrm{pH} \quad (4)$$

Acknowledgements

This work was funded by ERDF funds through the Portuguese Operational Programme for Competitiveness and Internationalization COMPETE 2020, and national funds through FCT–The Portuguese Foundation for Science and Technology, under the project "PTDC/CTM-ENE/2349/2014" (Grant Agreement No. 016660). The work is also partially funded by the Portugal-China Bilateral Collaborative Programme (FCT/21102/28/12/2016/S). L. F. L. acknowledges the financial support of the FCT Investigator Grant (IF/01595/2014) and Exploratory Grant (IF/01595/2014/CP1247/CT0001). L. Q. acknowledges the financial support of the Ministry of Science and Technology of China (No. 2016YFE0132400).

Electronic Supplementary Material: Supplementary material (UV–visible spectra of SiNW arrays and a planar Si; additional SEM images of SiNW@Co_2P-X; XRD patterns of SiNW@Co_2P; TEM-EDX spectra of a single SiNW@Co_2P; polarization curves of SiNW@Co_2P-X photocathodes; the dependence of J_0 and U_{onset} on the Co_2P loading; supporting table comparing the solar-driven HER performance of SiNW@Co_2P to those of other Si-based photocathodes reported in the literature) is available in the online version of this article at https://doi.org/10.1007/s12274-018-2070-4.

References

[1] Dincer, I. Renewable energy and sustainable development: A crucial review. *Renew. Sust. Energ. Rev.* **2000**, *4*, 157–175.

[2] Walter, M. G.; Warren, E. L.; McKone, J. R.; Boettcher, S. W.; Mi, Q. X.; Santori, E. A.; Lewis, N. S. Solar water splitting cells. *Chem. Rev.* **2010**, *110*, 6446–6473.

[3] Cook, T. R.; Dogutan, D. K.; Reece, S. Y.; Surendranath, Y.; Teets, T. S.; Nocera, D. G. Solar energy supply and storage for the legacy and nonlegacy worlds. *Chem. Rev.* **2010**, *110*, 6474–6502.

[4] Lewis, N. S.; Nocera, D. G. Powering the planet: Chemical challenges in solar energy utilization. *Proc. Natl. Acad. Sci. USA* **2006**, *103*, 15729–15735.

[5] Reece, S. Y.; Hamel, J. A.; Sung, K.; Jarvi, T. D.; Esswein, A. J.; Pijpers, J. J. H.; Nocera, D. G. Wireless solar water splitting using silicon-based semiconductors and earth-abundant catalysts. *Science* **2011**, *334*, 645–648.

[6] Sun, K.; Shen, S. H.; Liang, Y. Q.; Burrows, P. E.; Mao, S. S.; Wang, D. L. Enabling silicon for solar-fuel production. *Chem. Rev.* **2014**, *114*, 8662–8719.

[7] Candea, R. M.; Kastner, M.; Goodman, R.; Hickok, N. Photoelectrolysis of water-Si in salt-water. *J. Appl. Phys.* **1976**, *47*, 2724–2726.

[8] Thalluri, S. M.; Borme, J.; Xiong, D. H.; Xu, J. Y.; Li, W.; Amorim, I.; Alpuim, P.; Gaspar, J.; Fonseca, H.; Qiao, L. et al. Highly-ordered silicon nanowire arrays for photoelectrochemical hydrogen evolution: An investigation on the effect of wire diameter, length and inter-wire spacing. *Sustainable Energy Fuels* **2018**. DOI: 10.1039/C7SE00591A.

[9] Bao, X. Q.; Petrovykh, D. Y.; Alpuim, P.; Stroppa, D. G.; Guldris, N.; Fonseca, H.; Costa, M.; Gaspar, J.; Jin, C. H.; Liu, L. F. Amorphous oxygen-rich molybdenum oxysulfide decorated p-type silicon microwire arrays for efficient photoelectrochemical water reduction. *Nano Energy* **2015**, *16*, 130–142.

[10] Yuhas, B. D.; Smeigh, A. L.; Samuel, A. P. S.; Shim, Y.; Bag, S.; Douvalis, A. P.; Wasielewski, M. R.; Kanatzidis, M. G. Biomimetic multifunctional porous chalcogels as solar fuel catalysts. *J. Am. Chem. Soc.* **2011**, *133*, 7252–7255.

[11] Wang, J.; Zhong, H. X.; Wang, Z. L.; Meng, F. L.; Zhang, X. B. Integrated three-dimensional carbon paper/carbon tubes/cobalt-sulfide sheets as an efficient electrode for overall water splitting. *ACS Nano* **2016**, *10*, 2342–2348.

[12] Gholamvand, Z.; McAteer, D.; Backes, C.; McEvoy, N.; Harvey, A.; Berner, N. C.; Hanlon, D.; Bradley, C.; Godwin, I.; Rovetta, A. et al. Comparison of liquid exfoliated transition metal dichalcogenides reveals $MoSe_2$ to be the most effective hydrogen evolution catalyst. *Nanoscale* **2016**, *8*, 5737–5749.

[13] Zhang, L. M.; Liu, C.; Wong, A. B.; Resasco, J.; Yang, P. D. MoS_2-wrapped silicon nanowires for photoelectrochemical water reduction. *Nano Res.* **2015**, *8*, 281–287.

[14] Xiong, D. H.; Zhang, Q. Q.; Thalluri, S. M.; Xu, J. Y.; Li, W.; Fu, X. L.; Liu, L. F. One-step fabrication of monolithic electrodes comprising Co_9S_8 particles supported on cobalt foam for efficient and durable oxygen evolution reaction. *Chem.-Eur. J.* **2017**, *23*, 8749–8755.

[15] Chen, C. J.; Yang, K. C.; Basu, M.; Lu, T. H.; Lu, Y. R.; Dong, C. L.; Hu, S. F.; Liu, R. S. Wide range pH-tolerable silicon@pyrite cobalt dichalcogenide microwire array photoelectrodes for solar hydrogen evolution. *ACS Appl. Mater. Interfaces* **2016**, *8*, 5400–5407.

[16] Siracusano, S.; Baglio, V.; Grigoriev, S. A.; Merlo, L.; Fateev, V. N.; Aricò, A. S. The influence of iridium chemical oxidation state on the performance and durability of oxygen evolution catalysts in PEM electrolysis. *J. Power Sources* **2017**, *366*, 105–114.

[17] Wang, H. M.; Naghadeh, S. B.; Li, C. H.; Ying, L.; Allen, A. L.; Zhang, J. Z. Enhanced photoelectrochemical and photocatalytic activities of CdS nanowires by surface modification with MoS_2 nanosheets. *Sci. China Mater.* **2018**. DOI: 10.1007/s40843-017-9172-x.

[18] Ma, X. Y.; Li, J. Q.; An, C. H.; Feng, J.; Chi, Y. X.; Liu, J. X.; Zhang, J.; Sun, Y. G. Ultrathin Co(Ni)-doped MoS_2 nanosheets as catalytic promoters enabling efficient solar hydrogen production. *Nano Res.* **2016**, *9*, 2284–2293.

[19] Popczun, E. J.; McKone, J. R.; Read, C. G.; Biacchi, A. J.; Wiltrout, A. M.; Lewis, N. S.; Schaak, R. E. Nanostructured nickel phosphide as an electrocatalyst for the hydrogen evolution reaction. *J. Am. Chem. Soc.* **2013**, *135*, 9267–9270.

[20] Wang, X. G.; Kolen'ko, Y. V.; Bao, X. Q.; Kovnir, K.; Liu, L. F. One-step synthesis of self-supported nickel phosphide nanosheet array cathodes for efficient electrocatalytic hydrogen generation. *Angew. Chem., Int. Ed.* **2015**, *54*, 8188–8192.

[21] Roske, C. W.; Popczun, E. J.; Seger, B.; Read, C. G.; Pedersen, T.; Hansen, O.; Vesborg, P. C. K.; Brunschwig, B. S.; Schaak, R.

E.; Chorkendorff, I. et al. Comparison of the performance of CoP-coated and Pt-coated radial junction n$^+$p-silicon microwire-array photocathodes for the sunlight-driven reduction of water to H_2(g). *J. Phys. Chem. Lett.* **2015**, *6*, 1679–1683.

[22] Bao, X. Q.; Cerqueira, M. F.; Alpuim, P.; Liu, L. F. Silicon nanowire arrays coupled with cobalt phosphide spheres as low-cost photocathodes for efficient solar hydrogen evolution. *Chem. Commun.* **2015**, *51*, 10742–10745.

[23] Hellstern, T. R.; Benck, J. D.; Kibsgaard, J.; Hahn, C.; Jaramillo, T. F. Engineering cobalt phosphide (CoP) thin film catalysts for enhanced hydrogen evolution activity on silicon photocathodes. *Adv. Energy Mater.* **2016**, *6*, 1501758.

[24] Wang, X. G.; Li, W.; Xiong, D. H.; Petrovykh, D. Y.; Liu, L. F. Bifunctional nickel phosphide nanocatalysts supported on carbon fiber paper for highly efficient and stable overall water splitting. *Adv. Funct. Mater.* **2016**, *26*, 4067–4077.

[25] Li, W.; Gao, X. F.; Wang, X. G.; Xiong, D. H.; Huang, P. P.; Song, W. G.; Bao, X. Q.; Liu, L. F. From water reduction to oxidation: Janus Co-Ni-P nanowires as high-efficiency and ultrastable electrocatalysts for over 3,000 h water splitting. *J. Power Sources* **2016**, *330*, 156–166.

[26] Zhang, Y. T.; Chao, S. J.; Wang, X. B.; Han, H. J.; Bai, Z. Y.; Yang, L. Hierarchical Co_9S_8 hollow microspheres as multifunctional electrocatalysts for oxygen reduction, oxygen evolution and hydrogen evolution reactions. *Electrochim. Acta* **2017**, *246*, 380–390.

[27] Li, W.; Xiong, D. H.; Gao, X. F.; Song, W. G.; Xia, F.; Liu, L. F. Self-supported Co-Ni-P ternary nanowire electrodes for highly efficient and stable electrocatalytic hydrogen evolution in acidic solution. *Catal. Today* **2017**, *287*, 122–129.

[28] Wu, H. B.; Xia, B. Y.; Yu, L.; Yu, X. Y.; Lou, X. W. Porous molybdenum carbide nano-octahedrons synthesized via confined carburization in metal-organic frameworks for efficient hydrogen production. *Nat. Commun.* **2015**, *6*, 6512.

[29] Ma, B. J.; Xu, H. J.; Lin, K. Y.; Li, J.; Zhan, H. J.; Liu, W. Y.; Li, C. Mo_2C as non-noble metal Co-catalyst in Mo_2C/CdS composite for enhanced photocatalytic H_2 evolution under visible light irradiation. *ChemSusChem* **2016**, *9*, 820–824.

[30] Gong, Q. F.; Wang, Y.; Hu, Q.; Zhou, J. G.; Feng, R. F.; Duchesne, P. N.; Zhang, P.; Chen, F. J.; Han, N.; Li, Y. F. et al. Ultrasmall and phase-pure W_2C nanoparticles for efficient electrocatalytic and photoelectrochemical hydrogen evolution. *Nat. Commun.* **2016**, *7*, 13216.

[31] Yang, Y.; Wang, M.; Zhang, P. L.; Wang, W. H.; Han, H. X.; Sun, L. C. Evident enhancement of photoelectrochemical hydrogen production by electroless deposition of M-B (M = Ni, Co) catalysts on silicon nanowire arrays. *ACS Appl. Mater. Interfaces* **2016**, *8*, 30143–30151.

[32] Vrubel, H.; Hu, X. L. Molybdenum boride and carbide catalyze hydrogen evolution in both acidic and basic solutions. *Angew. Chem., Int. Ed.* **2012**, *51*, 12703–12706.

[33] Shalom, M.; Ressnig, D.; Yang, X. F.; Clavel, G.; Fellinger, T. P.; Antonietti, M. Nickel nitride as an efficient electrocatalyst for water splitting. *J. Mater. Chem. A* **2015**, *3*, 8171–8177.

[34] Bae, D.; Seger, B.; Vesborg, P. C. K.; Hansen, O.; Chorkendorff, I. Strategies for stable water splitting via protected photoelectrodes. *Chem. Soc. Rev.* **2017**, *46*, 1933–1954.

[35] Chandrasekaran, S.; Nann, T.; Voelcker, N. H. Nanostructured silicon photoelectrodes for solar water electrolysis. *Nano Energy* **2015**, *17*, 308–322.

[36] Dalchiele, E. A.; Martin, F.; Leinen, D.; Marotti, R. E.; Ramos-Barrado, J. R. Single-crystalline silicon nanowire array-based photoelectrochemical cells. *J. Electrochem. Soc.* **2009**, *156*, K77–K81.

[37] Jung, J. Y.; Choi, M. J.; Zhou, K. Y.; Li, X. P.; Jee, S. W.; Um, H. D.; Park, M. J.; Park, K. T.; Bang, J. H.; Lee, J. H. Photoelectrochemical water splitting employing a tapered silicon nanohole array. *J. Mater. Chem. A* **2014**, *2*, 833–842.

[38] Zhang, B. C.; Wang, H.; He, L.; Duan, C. Y.; Li, F.; Ou, X. M.; Sun, B. Q.; Zhang, X. H. The diameter-dependent photoelectrochemical performance of silicon nanowires. *Chem. Commun.* **2016**, *52*, 1369–1372.

[39] Sim, U.; Jeong, H. Y.; Yang, T. Y.; Nam, K. T. Nanostructural dependence of hydrogen production in silicon photocathodes. *J. Mater. Chem. A* **2013**, *1*, 5414–5422.

[40] Bazri, B.; Lin, Y. C.; Lu, T. H.; Chen, C. J.; Kowsari, E.; Hu, S. F.; Liu, R. S. A heteroelectrode structure for solar water splitting: Integrated cobalt ditelluride across a TiO_2-passivated silicon microwire array. *Catal. Sci. Technol.* **2017**, *7*, 1488–1496.

[41] Choi, S. K.; Piao, G. X.; Choi, W.; Park, H. Highly efficient hydrogen production using p-Si wire arrays and NiMoZn heterojunction photocathodes. *Appl. Catal. B-Environ.* **2017**, *217*, 615–621.

[42] Huang, Z. P.; Wang, C. F.; Pan, L.; Tian, F.; Zhang, X. X.; Zhang, C. Enhanced photoelectrochemical hydrogen production using silicon nanowires@MoS_3. *Nano Energy* **2013**, *2*, 1337–1346.

[43] Basu, M.; Zhang, Z. W.; Chen, C. J.; Chen, P. T.; Yang, K. C.; Ma, C. G.; Lin, C. C.; Hu, S. F.; Liu, R. S. Heterostructure of Si and $CoSe_2$: A promising photocathode based on a non-noble metal catalyst for photoelectrochemical hydrogen evolution. *Angew. Chem., Int. Ed.* **2015**, *54*, 6211–6216.

[44] Seger, B.; Pedersen, T.; Laursen, A. B.; Vesborg, P. C. K.; Hansen, O.; Chorkendorff, I. Using TiO_2 as a conductive protective layer for photocathodic H_2 evolution. *J. Am. Chem. Soc.* **2013**, *135*, 1057–1064.

[45] Seger, B.; Laursen, A. B.; Vesborg, P. C. K.; Pedersen, T.; Hansen, O.; Dahl, S.; Chorkendorff, I. Hydrogen production

using a molybdenum sulfide catalyst on a titanium-protected n plus p-silicon photocathode. *Angew. Chem., Int. Ed.* **2012**, *51*, 9128–9131.

[46] Bae, D.; Shayestehaminzadeh, S.; Thorsteinsson, E. B.; Pedersen, T.; Hansen, O.; Seger, B.; Vesborg, P. C. K.; Olafsson, S.; Chorkendorff, I. Protection of Si photocathode using TiO_2 deposited by high power impulse magnetron sputtering for H_2 evolution in alkaline media. *Sol. Energy Mater. Sol. Cell* **2016**, *144*, 758–765.

[47] Bao, X. Q.; Liu, L. F. Improved photo-stability of silicon nanobelt arrays by atomic layer deposition for efficient photocatalytic hydrogen evolution. *J. Power Sources* **2014**, *268*, 677–682.

[48] Tian, J. Q.; Liu, Q.; Asiri, A. M.; Sun, X. P. Self-supported nanoporous cobalt phosphide nanowire arrays: An efficient 3D hydrogen-evolving cathode over the wide range of pH 0–14. *J. Am. Chem. Soc.* **2014**, *136*, 7587–7590.

[49] Callejas, J. F.; Read, C. G.; Popczun, E. J.; McEnaney, J. M.; Schaak, R. E. Nanostructured Co_2P electrocatalyst for the hydrogen evolution reaction and direct comparison with morphologically equivalent CoP. *Chem. Mater.* **2015**, *27*, 3769–3774.

[50] Choi, S. K.; Chae, W. S.; Song, B.; Cho, C. H.; Choi, J.; Han, D. S.; Choi, W.; Park, H. Photoelectrochemical hydrogen production on silicon microwire arrays overlaid with ultrathin titanium nitride. *J. Mater. Chem. A* **2016**, *4*, 14008–14016.

[51] Zhang, C. T.; Pu, Z. H.; Amiinu, I. S.; Zhao, Y. F.; Zhu, J. W.; Tang, Y. F.; Mu, S. C. Co_2P quantum dot embedded N,P dual-doped carbon self-supported electrodes with flexible and binder-free properties for efficient hydrogen evolution reactions. *Nanoscale* **2018**, *10*, 2902–2907.

[52] Doan-Nguyen, V. V. T.; Zhang, S.; Trigg, E. B.; Agarwal, R.; Li, J.; Su, D.; Winey, K. I.; Murray, C. B. Synthesis and X-ray characterization of cobalt phosphide (Co_2P) nanorods for the oxygen reduction reaction. *ACS Nano* **2015**, *9*, 8108–8115.

[53] Blanchard, P. E. R.; Grosvenor, A. P.; Cavell, R. G.; Mar, A. X-ray photoelectron and absorption spectroscopy of metal-rich phosphides M_2P and M_3P (M = Cr-Ni). *Chem. Mater.* **2008**, *20*, 7081–7088.

[54] Huang, Z. P.; Zhong, P.; Wang, C. F.; Zhang, X. X.; Zhang, C. Silicon nanowires/reduced graphene oxide composites for enhanced photoelectrochemical properties. *ACS Appl. Mater. Interfaces* **2013**, *5*, 1961–1966.

[55] Sim, U.; Moon, J.; An, J.; Kang, J. H.; Jerng, S. E.; Moon, J.; Cho, S. P.; Hong, B. H.; Nam, K. T. N-doped graphene quantum sheets on silicon nanowire photocathodes for hydrogen production. *Energy Environ. Sci.* **2015**, *8*, 1329–1338.

[56] Esposito, D. V.; Levin, I.; Moffat, T. P.; Talin, A. A. H_2 evolution at Si-based metal-insulator-semiconductor photoelectrodes enhanced by inversion channel charge collection and H spillover. *Nat. Mater.* **2013**, *12*, 562–568.

[57] Hu, S.; Shaner, M. R.; Beardslee, J. A.; Lichterman, M.; Brunschwig, B. S.; Lewis, N. S. Amorphous TiO_2 coatings stabilize Si, GaAs, and GaP photoanodes for efficient water oxidation. *Science* **2014**, *344*, 1005–1009.

[58] Erlebacher, J. An atomistic description of dealloying-porosity evolution, the critical potential, and rate-limiting behavior. *J. Electrochem. Soc.* **2004**, *151*, C614–C626.